We are IntechOpen,
the world's leading publisher of
Open Access books
Built by scientists, for scientists

4,800
Open access books available

122,000
International authors and editors

135M
Downloads

Our authors are among the

154
Countries delivered to

TOP 1%
most cited scientists

12.2%
Contributors from top 500 universities

CLARIVATE ANALYTICS
BOOK CITATION INDEX
INDEXED

WEB OF SCIENCE™

Selection of our books indexed in the Book Citation Index
in Web of Science™ Core Collection (BKCI)

Interested in publishing with us?
Contact book.department@intechopen.com

Numbers displayed above are based on latest data collected.
For more information visit www.intechopen.com

Tracking Cellular Functions by Exploiting the Paramagnetic Properties of X-Nuclei

Eric Gottwald, Andreas Neubauer and
Lothar R. Schad

Additional information is available at the end of the chapter

Abstract

The term X-nuclei summarises all nuclei (except protons) that occur in biological systems carrying a non-zero nuclear spin. Significant involvement in physiological processes such as maintaining the transmembrane potential of living cells and energy metabolism make these nuclei highly interesting for nuclear magnetic resonance (NMR) experiments. In this chapter, a discussion of the basic physics of nuclei with a nuclear spin >1/2 is presented. On this basis, pulse sequences for the detection of multi quantum coherences (MQCs) are presented and explained. Information contained in the obtained MQC signal is linked to biophysical processes. Applications to study energy metabolism, oxygen consumption, and to track brain metabolites by means of X-nuclei NMR are discussed as well as the use of functional phantoms, which can bridge the gap between basic biological research and NMR data interpretation.

Keywords: sodium, potassium, chlorine, functional phantoms, X-nuclei

1. Introduction

Apart from hydrogen (^{1}H) all nuclei carrying a non-zero nuclear spin can be used for signal generation in nuclear magnetic resonance (NMR), magnetic resonance imaging (MRI), and magnetic resonance spectroscopy (MRS) experiments. All these nuclei are referred to by the term *X-nuclei*. Sodium (^{23}Na) is the X-nucleus with the highest NMR sensitivity, and thus, it was already used for imaging 30 years ago [1]. In addition to ^{23}Na, there are other X-nuclei, which can be used for MRI/MRS experiments. Together with potassium (^{39}K), ^{23}Na mainly determines the cell membrane potential. Chlorine (^{35}Cl) is the most abundant anion in the human body, and

its intracellular and extracellular concentrations have a huge impact on cell volume regulation. Oxygen (^{17}O) can give insight into the oxygen consumption of the tissue of interest. Phosphorus (^{31}P) is heavily involved in the energy metabolism (e.g. in skeletal muscle). Carbon (^{13}C) is the basis of all organic molecules and also enables the possibility to track brain metabolites. During the past years, several imaging techniques have been presented to exploit the signal of these nuclei [2].

The main question arising from the use of X-nuclei in MRI/MRS experiments is data interpretation. In biological systems, various processes are always occurring simultaneously, making it difficult to link a specific effect to an underlying physiological process. Therefore, methods are needed to bridge the gap between phantom experiments, which are used to develop new measurement techniques, and *in vivo* experiments. This can be accomplished with *functional phantoms* [3], which provide a high degree of control over biological processes, and therefore lead to a better understanding of the recorded signals.

This chapter gives an overview on the natural abundant X-nuclei, their physical properties, and physiological information, which can be obtained from NMR experiments with X-nuclei. Especially, the physics of X-nuclei with a nuclear spin >3/2 is discussed in detail with the goal to derive and understand enhanced pulse sequences for the observation of higher coherence orders. Applications for the spin 1/2 X-nuclei ^{17}O and ^{13}C are also discussed. The chapter closes with the introduction of a MRI compatible bioreactor setup, which can be used to study the response of organotypic cell cultures to external stimulations.

2. NMR sensitivity

Every nucleus used for NMR experiments has different physical properties and thus exhibits a different sensitivity response to radiofrequency (RF) pulses. The NMR sensitivity of a nucleus is given by:

$$S \propto C\gamma^3 I(I+1) \tag{1}$$

Here S is the sensitivity, C is the concentration of the nucleus, γ is the gyromagnetic ratio, and I represents the nuclear spin of the nucleus. Admittedly, most X-nuclei carry a nuclear spin > 1/2 which increases sensitivity. On the other hand, this effect is compensated by the much lower γ. Values for γ (relative to the value for ^{1}H), nuclear spin, natural abundances, and mean values of *in vivo* concentrations for the X-nuclei discussed here, are listed in **Table 1**. Since the nuclear spin and the gyromagnetic ratio are constants, the only variable in Eq. (1) is the concentration C. In contrast to ^{1}H, where the *in vivo* concentration reaches a molar (mol/l i.e. M) level, the concentrations of natural abundant X-nuclei is in the range of mM (mmol/l). For instance, ^{23}Na is the most abundant X-nucleus with the highest γ value but compared to ^{1}H the sensitivity is approximately 20,000 times lower.

Nucleus	Nuclear spin	Rel.γ	Natural abundance [%]	Mean *in vivo* concentration [mM]
^{1}H	1/2	1.00	99.98	88,000
^{13}C	1/2	0.25	1.11	n. a.
^{17}O	5/2	−0.14	0.037	16
^{23}Na	3/2	0.26	100.00	40
^{31}P	1/2	0.040	100.00	75
^{35}Cl	3/2	0.098	75.77	36
^{39}K	3/2	0.047	93.10	124

[1]Abundance in the whole body.

[2]Tissue ^{23}Na concentration in human brain.

[3]Tissue ^{35}Cl concentration in human brain.

[4]Concentration in human calf muscle. Since ^{13}C is mostly used for labelled precursors a value for *in vivo* concentration is lacking [4–8].

Table 1. Nuclear spin values, relative gyromagnetic ratios, natural abundances, and mean values of *in vivo* concentrations of different X-nuclei.

3. ^{23}Na, ^{35}Cl, and ^{39}K: interaction with proteins

The transmembrane potential mainly arises from concentration gradients of different ions between the intracellular and the extracellular compartments. Three X-nuclei, ^{23}Na, ^{35}Cl, and ^{39}K, and their intracellular/extracellular distribution play a major role in generating this potential. All three nuclei have a nuclear spin equal to 3/2, which leads to a nuclear quadrupolar moment Q and a fast decay of the NMR signal.

The nuclear quadrupolar moment is a measure of the deviation of the nuclear charge distribution from the spherical shape. Positive values of Q indicate, that the nuclear charge distribution takes the shape of a prolate spheroid while negative values indicate, that the nucleus takes the form of an inflate spheroid. The values for Q and the resulting shape of the discussed nuclei are listed in **Table 2**.

Nucleus	Quadrupolar moment Q [b]	Shape
^{17}O	−0.026[*]	Inflate spheroid
^{23}Na	+0.10[*]	Prolate spheroid
^{35}Cl	−0.10[*,†]	Inflate spheroid
^{39}K	+0.049[*,†]	Prolate spheroid

[*]Polarization or Sternheimer corrections incorporated.

[†]Average value [9].

Table 2. Quadrupolar moments and shapes of nuclei with nuclear spin >1/2.

The quadrupolar moment also implicates an additional electrical field which, in turn, leads to an additional contribution to the potential energy of the nucleus. This means that the energy levels, which split due to the Zeeman effect,[1] will be shifted due to the quadrupolar interaction, ω_Q, which is related to the electrical field induced by the quadrupolar moment. A description of the electrical field can be formulated using of the electrical field gradient (EFG) tensor, which can be found in references [10, 11]. **Figure 1** shows an illustration for the Zeeman effect in case of a spin 3/2 nucleus. On the left hand side of the figure, there is no external magnetic field and the energy levels are degenerate. Applying an external magnetic field nulls the degeneration and the energy levels split. In biological systems, the quadrupolar interaction can become time dependent. Therefore, it is useful to refer to the time averaged quadrupolar interaction $\langle \omega_Q \rangle$. For a non-zero external magnetic field and $\omega_Q = 0$, this is shown in the middle of **Figure 1**. The right hand side of **Figure 1** shows the case with an applied external magnetic field, where $\omega_Q \neq 0$. It can be seen that the inner transitions are shifted to lower energies while the outer transitions are shifted to higher energies. This leads to an alteration of the transition frequencies for the outer transitions.
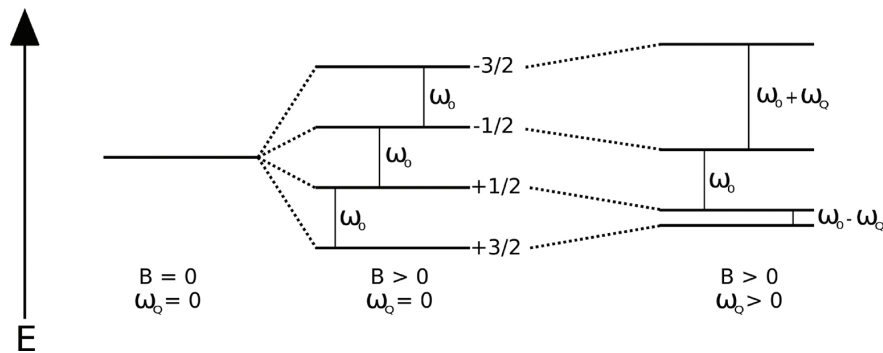

Figure 1. Zeeman effect in a spin 3/2 system. (Left) In the absence of an external magnetic field, the energy levels are degenerated. (Middle) Application of an external magnetic field leads (in the absence of a quadrupolar interaction) to an equidistant splitting of the energy levels. (Right) An additional quadrupolar interaction leads to a shift of the inner levels towards lower energy while the outer levels are shifted upwards. The end result is an alteration of the outer transitions.

The following paragraphs contain the description of the physical properties of signal generation and relaxation these nuclei. From this basis, dedicated pulse sequences for the observation of *multi quantum coherences* (MQCs) are derived. Applications of these sequences to phantoms are shown while the obtained data are analysed with the link to a physiological interpretation.

3.1. Quadrupolar relaxation

This section deals with the specific relaxation processes of quadrupolar nuclei. The detailed understanding of these processes requires a strong background in quantum physics, and the use of the irreducible tensor formalism which is beyond the scope of this book. For this reason, only the key results of the quantum mechanical description are presented in this chapter. The reader can find a more detailed description in references [10–12].

Taking this into account one can deduce the following two respective expressions for the real and imaginary parts (J_m and K_m) of the spectral density [11]:

$$J_m\left(m\omega_0\right)=\frac{\left(2\pi\right)^2}{20}\frac{\chi^2\tau_c}{1+\left(m\omega_0\tau_c\right)^2} \tag{2}$$

$$K_m\left(m\omega_0\right)=\omega_0\tau J_m\left(m\omega_0\right) \tag{3}$$

In the latter equations, ω_0 is the resonance frequency, τ is the length of the excitation pulse, τ_c is the rotational correlation time, which is a measurement for the degree of freedom of a nucleus, χ represents the root mean square coupling constant, and m is an integer number, which will be discussed later. Since no other correlation time will be discussed in this chapter, the rotational correlation time will be referred only as correlation time.

If nuclei can move freely, like in isotropic liquids, the correlation time is rather small and in the range of ns. If the motion becomes more restricted, like it is the case during the interaction with macromolecules, such as proteins, the correlation time increases. The quadrupolar coupling constant ω_Q is accounted for in the spectral density via the parameter χ. In biological systems, there is an increased variability of different environments and simultaneously ongoing processes leading to local variations of ω_Q, which justifies the usage of the root mean square value χ.

The influence of τ_c and ω_Q on the spectral density was extensively discussed by Rooney et al. [13]. In their paper, they defined four different regimes for τ_c and ω_Q resulting in four different types of spectra which are shown in **Figure 2**. These four regimes are:

- *Type a spectrum:* $\omega_Q\tau_c \gg 1$ and $\omega_0\tau_c \gg 1$ and an additional macroscopic anisotropy in the sample (e.g. single or liquid crystals). Molecular motion is hardly present in this system which leads to distinct energy levels and three very narrow resonances comprising the central resonance and two symmetrical satellite resonances at higher and lower frequencies, respectively

- *Type b spectrum:* $\omega_Q\tau_c \gg 1$ and $\omega_0\tau_c \gg 1$ and a random distribution of the orientation of the EFG tensors (e.g. inhomogeneous powder). Similar to the case of type a, molecular motion is hardly present but the random distribution of the EFG tensors leads to a broadening of the energy levels. In contrast to type a, where the spectrum shows three sharp lines, the satellite transitions become broadened due to many different values for ω_Q, and form a powder spectrum

- *Type c spectrum:* $\omega_Q\tau_c \ll 1$ and $\omega_0\tau_c > 1$ and restricted motion (e.g. due to the interaction with proteins). In this type, the molecular motion is much higher than in the latter two. As a result, the energy levels are continually modulated and the satellite transitions vanish. As it can be seen (second column from the left) in **Figure 2** , the satellite resonances are completely vanished and the central resonance takes the shape of a Lorentzian which is also influenced

by the orientation of the different EFG tensor orientations with respect to the external magnetic field (super-Lorentzian)

- *Type d spectrum:* $\langle \omega_Q \rangle = 0$ and $\omega_0 \tau_c \ll 1$. This is the case in isotropic liquids. Due to rapid molecular motion, the time average of the quadrupolar interaction vanishes and the energy levels become sharp again. Moreover, there is no difference between the different transitions leading to a single, sharp resonance at ω_0
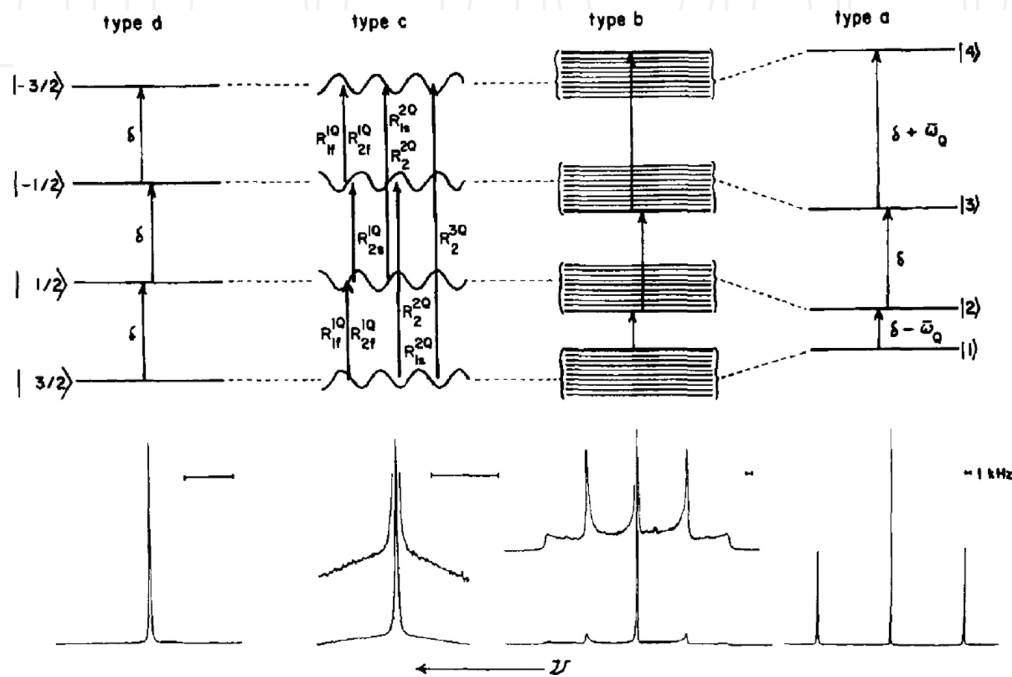

Figure 2. The four possible regimes for ^{23}Na spectra according to Rooney et al. Figure drawn from reference [13]. Copyright permission by John Wiley & Sons Ltd (license no. 3824201099423).

As it can be seen in **Figure 2**, nuclei with a nuclear spin > 1/2 can exhibit more than just one resonance. Therefore, transitions equal multiple times of the resonance frequency are possible. These transitions are known as *multi quantum coherences (MQCs)*. In the case of spin 3/2 nuclei, single quantum (SQ) coherences can be observed, which are normally used for proton MRI and two MQCs, double quantum (DQ) coherences and triple quantum (TQ) coherences, respectively. In order to understand the relaxation properties of SQ coherences, a homogeneous and isotropic environment with only one compartment is assumed. The detailed discussion of higher coherences will be treated separately.

3.1.1. Longitudinal relaxation

As known from ^{1}H-NMR the specific time constant T_1 for the longitudinal relaxation can be determined by usage of an inversion recovery (IR) sequence. After an initial 180° pulse follows an evolution period called inversion time (T_i). Observable magnetization is then generated by an additional 90° excitation pulse.

If the time between the last pulse and the acquisition is kept minimal, the acquired signal can be formulated according to reference [11]:

$$S\left(S_0, T_i\right) = S_0\left(1 - \frac{2}{5}\left(e^{-R_1^0 T_i} + 4e^{-R_2^0 T_i}\right)\right)$$ (4)

with S_0, the signal which can be obtained in the case $T_i = 0$, and with the relaxation rates

$$R_1^0 = 2J_1$$ (5)

$$R_2^0 = 2J_2$$ (6)

While the relaxation rates R_1^0 and R_2^0 are given by the spectral densities J_1 and J_2 [11]:

$$J_1 = \frac{(2\pi)^2}{20} \frac{\chi^2 \tau_c}{1 + (\omega_0 \tau_c)^2}$$ (7)

$$J_2 = \frac{(2\pi)^2}{20} \frac{\chi^2 \tau_c}{1 + (2\omega_0 \tau_c)^2}$$ (8)

Here, it should be pointed out that the integer m, which was mentioned in the definition of the spectral densities (see Eqs. (2) and (3)), takes the values of 1 and 2. Theoretically, a biexponential relaxation curve which contains a fast and a slow relaxing component can be observed. However, it is very difficult to observe a biexponential T_1 relaxation, especially in biological tissue. Nevertheless, for ^{35}Cl a biexponential T_1 relaxation has been observed *in vivo* [14, 15].

It is common to express the relaxation rates with their inverse value, which leads to two different time constants:

$$T_{1f} = \frac{1}{R_1^0}$$ (9)

$$T_{1s} = \frac{1}{R_2^0}$$ (10)

T_{1f} depicts the time constant for the fast, and T_{1s} for the slow relaxing component. In the extreme narrowing limit $\omega_0 \tau_c \ll 1$ (i.e. isotropic liquid), it follows that $T_{1f} = T_{1s}$. Therefore, the relaxation becomes monoexponential with the time constant T_1 and the signal equation simplifies to

$$S(S_0, T_i) = S_0 \left(1 - 2e^{\frac{-T_i}{T_1}} \right) \tag{11}$$

3.1.2. Transverse relaxation

To measure the characteristic time constant T_2 for the longitudinal relaxation, spin echo (SE) sequences are commonly used. These sequences begin with an initial 90° excitation pulse. Subsequent to this pulse a 180° inversion pulse is placed in the middle of an evolution interval called echo time (T_E).

A more detailed version of the following description for the elicited SE signal can be found in reference [11]. The SE signal takes the form:

$$S(S_0, T_E) = S_0 \frac{1}{5} \left(3e^{-R_1^1 T_E} + 2e^{-R_2^1 T_E} \right) \tag{12}$$

S_0 is the signal intensity when T_E is minimal and the relaxation rates are represented by:

$$R_1^1 = J_0 + J_1 \tag{13}$$

$$R_2^1 = J_1 + J_2 \tag{14}$$

In this case, the spectral density with m = 0 equals

$$J_0 = \frac{(2\pi)^2}{20} \chi^2 \tau_c \tag{15}$$

where J_1 and J_2 are the same spectral densities defined in Eqs. (7) and (8). Expressing the relaxation rates with their inverse and leads to

$$T_{2f} = \frac{1}{R_1^1} \tag{16}$$

$$T_{2s} = \frac{1}{R_2^1}$$
(17)

Similar to the case of T_1 relaxation, the T_2 relaxation is biexponential and consists of a fast relaxing component with relaxation time T_{2f} and a slow relaxing component with a relaxation time T_{2s}. In the extreme narrowing limit, the relaxation times become equal and lead to a monoexponential relaxation. In contrast to longitudinal relaxation, the two components of the transverse relaxation can be measured straight forward. Examples can be found in references [14, 15].

3.1.3. Rotational correlation time and its influence on relaxation times

As referred to in the discussion of longitudinal and transverse relaxation time, the rotational correlation time τ_c, and the root mean square value of the quadrupolar interaction constant χ appear in each of these two processes. The relaxation rates of longitudinal and transverse relaxation can be used to determine τ_c and χ in a model with a single compartment. However, since the biexponential behaviour can be observed much easier in transverse relaxation, the relaxation rates R_1^1 and R_2^1 are used here to determine τ_c and χ. Additionally, the substitution $x = (\omega_0 \tau_c)^2$ is used.

First, the ratio a_1 of the two relaxation rates can be calculated as

$$a_1 = \frac{R_1^1}{R_2^1} = \frac{(2+x)(1+4x)}{2+5x}$$
(18)

Rearranging Eq. (18) for τ_c leads to:

$$\tau_c = \frac{1}{\omega_0} \sqrt{\frac{-9 + 5a_1 \pm \sqrt{25a_1^2 - 58a_1 + 49}}{8}}$$
(19)

Knowledge of τ_c can then be used to calculate the value for χ. Herein, the first step is to compute the difference b_1 of the relaxation rates:

$$b_1 = R_1^1 - R_2^1 = \frac{4\pi^2}{5} \chi^2 \tau_c \frac{x}{1+4x}$$
(20)

Solving for χ leads to,

$$\chi = \frac{1}{2\pi} \sqrt{\frac{5b_1(1+4x)}{\tau_c x}} \tag{21}$$

In order to study the behaviour of the relaxation times under the influence of τ_c, a constant value for χ is assumed. From Eq. (19) follows that τ_c depends on the resonance frequency and thus on the magnetic field strength, leading to a dependence of all relaxation times on the magnetic field strength. **Figure 3** shows the simulated behaviour of the product of T_1 and T_2 with χ being dependent on τ_c for magnetic field strengths of 9.4 T and 21.1 T. For the longitudinal relaxation, the assumed monoexponential behaviour leads to a single longitudinal relaxation time constant T_1. In case of the transverse relaxation, a biexponential behaviour was assumed, which leads to a fast relaxing (T_{2f}) and a slow relaxing (T_{2s}) component of the transverse relaxation time constant T_2. The value for τ_c, where the product $\omega_0\tau_c = 1$, is indicated with the dotted red lines for both field strengths. At increasing correlation times, it can be clearly seen that the fast transverse relaxation time is continuously decreasing. Time constants for longitudinal relaxation as well as the constants for slow transverse relaxation first decrease at an increasing correlation time. Around the area $\omega_0\tau_c = 1$, the relaxation times start to increase again. This clarifies why the value for longitudinal relaxation times in solids is of the order of seconds, whereas it is in the range of milliseconds for liquids.
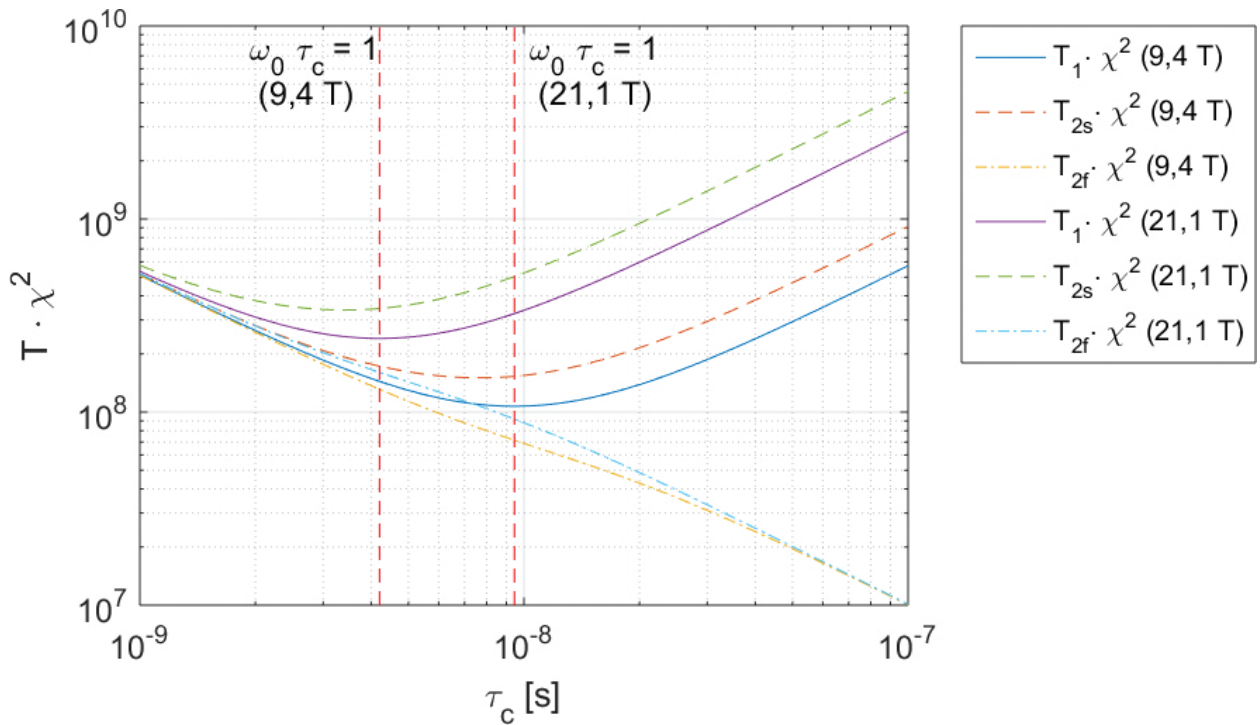

Figure 3. Dependence of relaxation times on the correlation time. Longitudinal as well as the slow components of transverse relaxation times initially decrease at increasing correlation times. Above the extreme narrowing limit, these relaxation times increase again. Short components of transverse relaxation times fall continuously at increasing correlation times.

3.1.4. Multi quantum coherences

As mentioned earlier, X-nuclei with a nuclear spin > 1/2 can exhibit MQCs. The theoretical description of MQCs is very complex and requires a background in quantum mechanics, a formulation that is outside the scope of this book. However, very extensive descriptions can be found in references [11, 16, 17].

MQCs can be a valuable tool for providing physiological information in MRI experiments. X-nuclei such as ^{23}Na, ^{35}Cl, and ^{39}K, which are heavily involved in physiological processes possess a nuclear spin equal to 3/2, and can therefore be used to generate MQCs. **Figure 4** shows all possible coherences in a spin 3/2 system. SQ and DQ coherences can be found in liquids as well as in environments with restricted motion. The most specific coherence is the TQ coherence. This coherence can only be found above the extreme narrowing limit $\omega_0\tau_c \geq 1$, which can only be reached when there is at least temporary binding. In biological systems, this is realized by the interaction with macromolecules, such as proteins. For that reason, the intensity of the TQ signal can give insight in the amount of interaction between ions and proteins. Therefore, the sequences presented subsequently, exclusively deal with the generation and detection of SQ and TQ coherences.
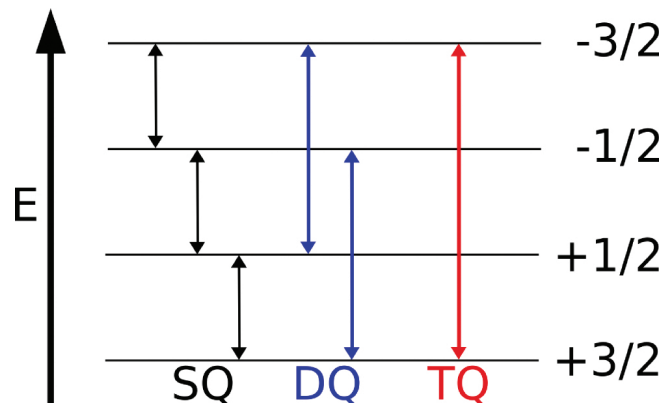

Figure 4. Multi quantum coherences in a spin 3/2 system. (Black) single quantum (SQ) transitions occur between neighbouring levels. (Blue) Double quantum (DQ) transitions skip one energy level. (Red) triple quantum (TQ) transitions skip two energy levels.

If pulsed excitation is used, like in common NMR spectrometers or MRI scanners, it is not possible to record MCQs directly. Instead of direct excitation with a single RF pulse, several excitation pulses need to be applied to generate a signal which includes MCQs. Typically, the signal generated by MCQs is much weaker than signal generated SQ coherences. As a result, one has to apply filter techniques to suppress contributions from unwanted coherences. There are two ways to filter different coherences: either through the application of gradient pulses, or by cycling the phases of applied pulses and/or the receiver.

Usage of gradient pulses is associated with the advantage of short total measurement times but the signal intensity is reduced by a factor of two. If phase cycling is used, the sequence must be repeated several times, each time with a different set of pulses and/or receiver phases.

If one deals with TQ coherences, the avoidance of signal loss is often more important than saving scanning time. For this reason, phase cycling is the preferred method in this chapter. Nevertheless, the reader can find some examples for filtration with gradient pulses in reference [18].

A common method for exciting and detecting TQ coherences is a pulse scheme consisting of three 90° excitation pulses, as illustrated in **Figure 5**. As it can be seen, all pulses have the same amplitude, while the phases of the first two pulses can vary. The time period between the first and the second pulse is called evolution time τ_{Evo}, and it is typically within the range of ms. Between the second and the third pulse, there is another short delay called mixing time, τ_{Mix}, which is typically in the range of several μs. In the case of TQ filtration, Φ' is set to 90° while Φ is cycled through the values of 30°, 90°, 150°, 210°, 270° and 330°. In addition to this, the receiver phase is altered between 0° and 180° after each subsequent scan and the phase of the third pulse is constantly equal to 0°. During the second pulse of the phase cycle, each coherence will accumulate the phases linearly, according to the number of energy levels which where skipped, i.e. DQ coherences will accumulate the phase with a factor one, and TQ coherences with a factor of two, respectively. In the literature, this is referred to as *triple quantum filtered T_2 (TQF-T_2)* experiment, or simply, a TQF experiment.
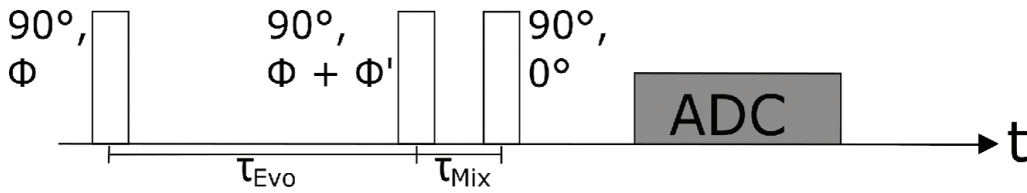

Figure 5. Three-pulse scheme for excitation and detection of MCQs. Pulse phases are indicated with Φ and Φ'. The time delays τ_{Evo} and τ_{Mix} represent evolution and mixing time. Data acquisition is indicated with ADC which refers to the analogue-to-digital converter.

The actual signal is obtained by complex addition of all subsequent scans. **Table 3** shows the phases accumulated by all coherences during the TQF experiment. As it can be seen from the values listed in **Table 3**, the contribution from SQ and DQ coherences cancel each other out while the phases of the TQ contributions are constant. After addition, the TQ signal can be expressed with the following equation [11]:

$$S\left(\tau_{Evo}\right) = \frac{15}{16} \frac{\sqrt{6}}{5} \left(e^{-R_1^1 \tau_{Evo}} - e^{-R_2^1 \tau_{Evo}} \right) \tag{22}$$

The relaxation rates R_1^1 and R_2^1 were defined in Eqs. (13) and (14). To avoid the influence of the acquisition time of the generated free induction decay (FID), a Fourier transform (FT) can be performed along the acquisition time domain. The dependence of τ_{Evo} is then found at ω_0 along the direction of τ_{Evo}.

SQ	DQ	TQ
30°	150°	270°
90°	90°	270°
150°	30°	270°
210°	330°	270°
270°	270°	270°
330°	210°	270°

Table 3. Accumulated phases of the different coherences during the TQF experiment.

Situations with $\omega_0 \tau_c \geq 1$ can be easily simulated using solutions and the addition of agarose. The more agarose the sample contains, the higher the correlation time. In order to simulate different *in vivo* situations the agarose concentration can be varied from 1 to 7.5%. From this data, the correlation time can be extracted according to the one compartment model. This phantom data can help to interpret *in vivo* data regarding to the degree of ion binding. **Figure 6** shows the TQF signals of ^{23}Na in samples with different agarose concentration and 154 mM ^{23}Na concentration in dependence of the evolution time τ_{Evo} recorded at 9.4 T. All curves were normalized after acquisition and fitted according to the signal equation. With increasing agarose levels, one can clearly see an increase in the *signal-to-noise ratio (SNR)* indicating that the interaction of the ^{23}Na ions with their environment is also increasing. Additionally, the curves exhibit faster rise and decay times with increasing agarose, which is equivalent to an increase in both relaxation rates and a decrease in both relaxation times, respectively.
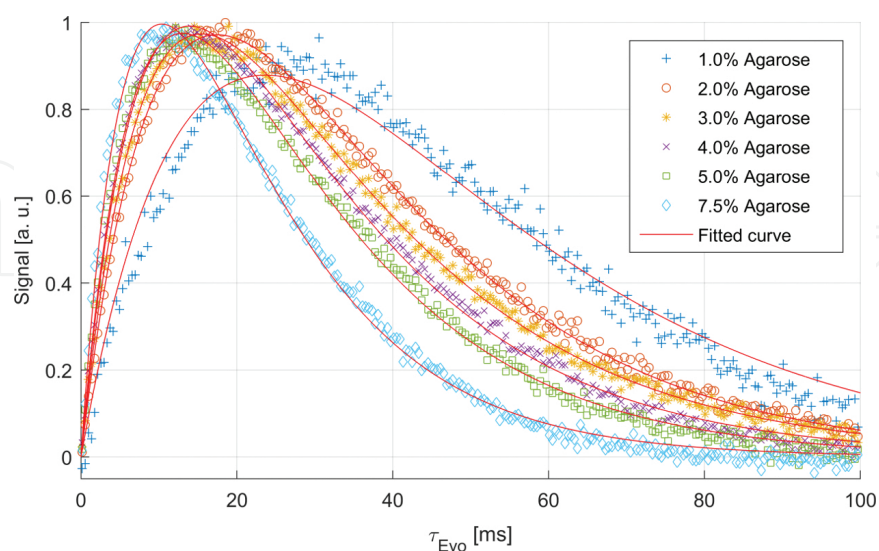

Figure 6. TQF signal of ^{23}Na at different agarose concentrations as a function of τ_{Evo} at 9.4 T. Increasing agarose content leads to an increased interaction between ^{23}Na and its environment, therefore, the TQF signal also increases. Additionally, both relaxation times become shorter, leading to a more rapid rise and decay of the signal.

As previously mentioned, the degree of binding will lead to an increase in TQ contributions.

If one wants to record dynamic processes, such as changes in the amount of free water or ion concentrations, a reference is needed. In *in vivo* experiments, it is often difficult to work with an external reference which underlies variations in transmit and receive fields. It would be more accurate to generate a spectrum with an intrinsic reference. In case of ^{1}H-MRS or ^{31}P-MRS, a spectrum with multiple peaks arises from different binding partners of the nucleus under observation. Unfortunately, X-nuclei with nuclear spin > 1/2 hardly have permanent binding partners. In most cases, the binding is related to interactions with macromolecules and cannot be seen in conventional spectroscopy.

SQ	DQ	TQ
90°	270°	90°
90°	90°	90°
135°	0°	225°
135°	180°	225°
180°	90°	0°
180°	270°	0°
225°	180°	135°
225°	0°	135°
270°	270°	270°
270°	90°	270°
315°	0°	45°
315°	180°	45°
0°	90°	180°
0°	270°	180°
45°	180°	315°
45°	0°	315°

Table 4. Phases of different coherences by applying triple quantum filtered time proportional phase increment (TQTPPI) spectroscopy with DQ suppression.

The solution to this problem is provided by multi quantum (MQ) spectroscopy. A very promising sequence to generate more resonance peaks from different MQCs in a single spectrum is referred to with the term *triple quantum filtered time proportional phase increment (TQTPPI)* [19]. The sequence diagram is basically the same shown in **Figure 5**. The only

difference is the applied phase cycle and the fact that τ_{Evo} is incremented after each step in the phase cycle. Since DQ coherences also occur in liquids, a suppression of these contributions can help to simplify the signal and can be achieved by application of a 16 step phase cycle starting with $\Phi = 90°$, for the first pulse. The second pulse carries the variable phase Φ and the constant phase $\Phi' = 90°$ and the phase of the third pulse is, like the receiver phase, equal to zero. In order to suppress DQ coherences, each step in the phase cycle has to be repeated twice, the second time with an additional 180° phase on the middle pulse. Incrementing Φ and τ_{Evo} is then performed after each second step in the phase cycle. Typical values for Φ and τ_{Evo} are 45° and 100 μs. **Table 4** shows the resulting phases of all occurring coherences after application of the 16 step phase cycle. It can be seen that in the case of SQ and TQ contributions, the phases of two subsequent scans are equal, while the two subsequent phases for DQ contributions differ by 180°. DQ suppression can then be achieved by the addition of the two subsequent scans.
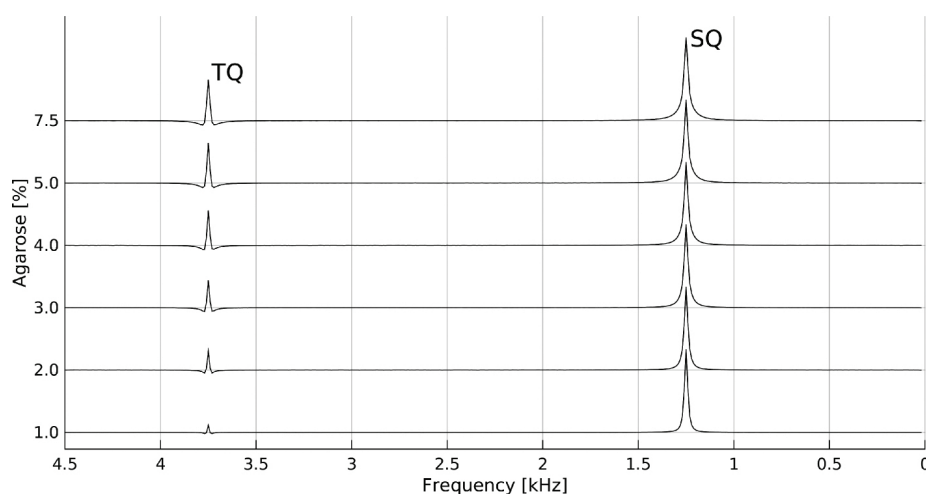

Figure 7. TQTPPI spectra of ^{23}Na at 9.4 T with different concentrations of agarose. The frequency increases from right to left. All curves were normalized with respect to the SQ resonance. At increasing agarose content (shown along the y-axis), the TQ contribution becomes more pronounced.

Generating the desired signal includes two steps: First, a FT has to be performed in the acquisition domain. Second, a second FID is generated by taking the points at ω_0 in the evolution time domain. This second dimension FID can be therefore turned into a spectrum by the application of an additional FT. Only the experimental results of this sequence are shown. Interested readers can find a very detailed derivation of the signal equation in reference [17].

Figure 7 shows TQTPPI spectra with DQ suppression of ^{23}Na obtained at 9.4 T. Different agarose concentrations are located along the y-axis. The first peak from the right is the SQ resonance which is located at 1.25 kHz. Accordingly, the TQ resonance appears at a frequency of 3.75 kHz which is exactly three times the SQ frequency. All of the spectra are normalized to the maximum value of the SQ resonance. One can clearly see the gain in TQ signal at increasing agarose concentrations. It is possible to consider the SQ peak as an internal reference, to

calculate the area under both peaks and to build the ratio TQ/SQ. Observing the TQ/SQ ratio allows the conduct of dynamic studies of changes in the motional freedom induced by changes in the binding of the nucleus under investigation. If applied to biological tissue, this can give valuable information about the amount of bound ions and their interaction with proteins in the tissue.

3.2. ^{31}P: Energy metabolism

^{31}P spectroscopy has found its way into basic and clinical research due to the fact that ^{31}P is involved in energy metabolism. Energy consuming processes, such as the maintenance of the membrane potential, use the hydrolysis of adenosine triphosphate (ATP) as the energy source. The reaction is in accordance to:
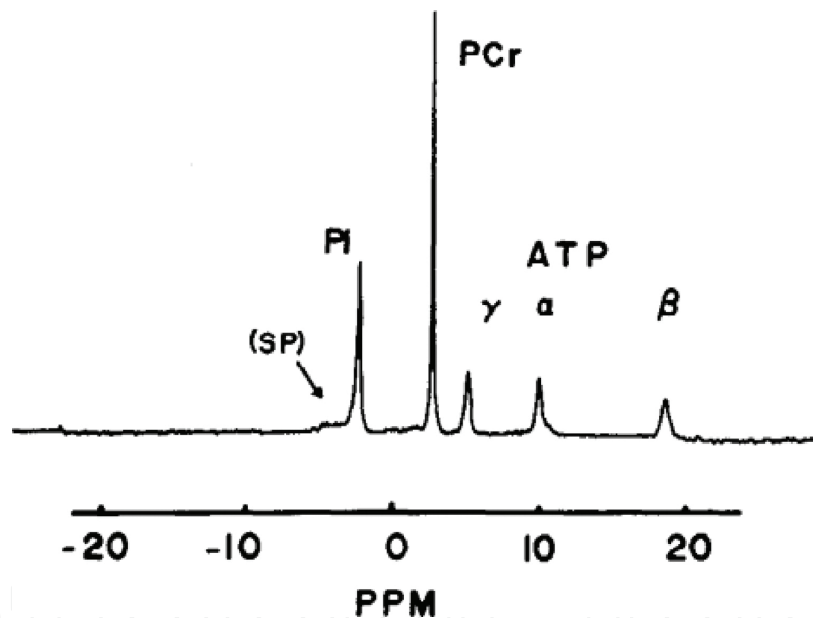
$$ATP + H_2O \rightarrow ADP + P_i \tag{23}$$

Figure 8. ^{31}P spectrum of a resting, arterially perfused cat soleus muscle. One can clearly see the phosphocreatine (PCr) resonance. The α, β, and γ resonances of adenosine triphosphate (ATP) are found at positive values for δ, while the inorganic phosphate (Pi) resonates at negative δ values. Contributions of sugar phosphate (SP) are also found at negative δ values. Figure drawn from reference [20]. Copyright permission by The American Physiological Society (license no. 3871910770507).

It can be seen that adenosine diphosphate (ADP) and inorganic phosphate (Pi) are produced during this reaction. In addition to the resonances of ATP, ADP and Pi one can also detect ^{31}P resonances from phosphomonoesters and diesters. **Figure 8** shows an example for a ^{31}P spectrum recorded from a resting, arterially perfused cat soleus muscle [20]. One can clearly see the three resonances of ATP, the phosphocreatine (PCr) resonance, and the resonance line of Pi. Small contributions from sugar phosphate (SG) are also visible.

An overview of resonances of detectable metabolites is shown in **Table 5** [4]. As it can be seen from **Table 5**, the chemical shift (δ) of the different metabolites covers a wide range. By convention, the PCr resonance is set as internal reference ($\delta = 0.00$ ppm).

Metabolite	Chemical shift
Adenosine monophosphate (AMP)	6.33
Adenosine diphosphate (ADP)	-7.05 (α)
	-3.09 (β)
Adenosine triphosphate	-7.52 (α)
	-16.26 (β)
	-2.48 (γ)
Dihydroxyacetone phosphate	7.56
Glucose-1-phosphate	5.15
Glucose-6-phosphate	7.20
Inorganic phosphate (P_i)	5.02
Phosphocreatine (PCr)	0.00
Phosphoenolpyruvate	2.06
Phosphoryl choline	5.88
Phosphoryl ethanolamine	6.78
Nicotinamide adenine dinucleotide (NADH)	-8.30

Table 5. Detectable metabolites by ^{31}P spectroscopy with their chemical shift.

In ^{31}P applications, it is not only possible to measure the concentration of a metabolite, it is also possible to derive rate constants based on changes of the concentrations of the PCr, Pi, and ATP. To influence the concentrations of PCr, Pi, and ATP, it is common to acquire the data while a volunteer is exercising and during the recovery period after the exercise. In the literature, one can find a variety of studies of the energy metabolism of human calf muscles. An extensive review is presented in reference [21].

The fact that the chemical shift of many ^{31}P resonances is dependent on the intracellular pH and magnesium concentration, leads to another interesting application, namely, the *in vivo* measurement of pH values. This can be achieved using the Henderson-Hasselbach equation:

$$pH = pK + log\left(\frac{\delta - \delta_{HA}}{\delta_A - \delta}\right) \tag{24}$$

where *pK* is the equilibrium constant for the acid-base equilibrium between A and HA. The chemical shifts of the protonated and dissociated forms of the molecule under observation are expressed by δ_{HA} and δ_A, respectively. Determining pH is achieved by measuring the chemical shift δ between PCr and Pi. With literature values, Eq. (24) takes the form [22]:

$$pH = 6.803 + log\left(\frac{\delta - 3.22}{5.73 - \delta}\right) \tag{25}$$

3.3. ^{17}O: Oxygen consumption

Supplying living cells with oxygen is of crucial importance for their viability. This can be seen by the huge impact a shortage of oxygen (hypoxia) has on, for example, brain functions. In order to access the production of NMR visible $H_2^{17}O$, the paramagnetic properties of ^{17}O can be used. There are two ways to use ^{17}O in magnetic resonance (MR) experiments.

Firstly, with direct detection of the ^{17}O resonance, and secondly, by use of the change in the ^{1}H relaxation times due to the coupling between ^{17}O and ^{1}H. Direct and indirect detections suffer from the low natural abundance of ^{17}O of 0.037%. Together with low values for γ, this leads to a sensitivity which is a factor of 1.7×10^5 lower than for ^{1}H. To overcome this obstacle, techniques for increasing the ^{17}O concentration are highly valuable. For this purpose, setups, like those listed in reference [23], for the inhalation of ^{17}O enriched gas which can increase the ^{17}O concentration above the natural abundance, are continuously developed.

As mentioned, a concentration increase can be reached by the inhalation of ^{17}O enriched gas. After inhalation, the oxygen binds to haemoglobin due to lung exchange and is transported to the brain via the vascular system. As long as the oxygen gas is bound to haemoglobin, it is practically NMR invisible. In this state, the rotational motion is very slow leading to a very low value for τ_c and therefore to a rapid transverse relaxation. Through cerebral oxygen metabolism (CMRO$_2$), NMR observable ^{17}O enriched water is produced according the following equation:

$$4H^+ + 4e^- + {}^{17}O_2 -> 2H_2{}^{17}O \tag{26}$$

According to references [10] and [24], the relaxation rates R_1 and R_2 for the ^{17}O nucleus in tissue water within the extreme narrowing limit can be estimated as follows:

$$R_2 = \frac{1}{T_2} \cong R_1 = \frac{1}{T_1} = 1.056\chi^2\tau_c \tag{27}$$

where χ is the root mean square coupling constant introduced in Eq. (2). Under coupling to ^{17}O, the transverse relaxation rate $R_{2,H}$ of the ^{1}H nucleus can be estimated as follows:

$$R_{2,H} = \frac{1}{T_{2,H}} \approx \frac{1}{T_{2,H}^{O}} + \frac{35}{12} P\tau J^2 \tag{28}$$

The relaxation time T_{2H}^{O} denotes the transverse relaxation time for ^{1}H when it is bound to ^{16}O, P is the molar fraction for H_2[17]O which is equivalent to the [17]O enrichment factor, τ is in this case the characteristic proton exchange lifetime and J^2 is the scalar [17]O-^{1}H coupling constant. Hopkins et al. have shown that only the transverse and not the longitudinal relaxation is influenced by the presence of [17]O enriched water [25].

3.4. [13]C: Brain metabolites

Like all organic compounds, brain metabolites are consisted of carbon atoms and protons. Therefore, for MRS experiments, it is sensible to consider the carbon isotope ^{13}C, which carries a nuclear spin equal to 1/2. From **Table 1** follows that the value for γ is just 25% of the proton value. Given the low natural abundance of 1.1%, it also has a relatively low NMR sensitivity. If a carbon spectrum is recorded at natural abundance, it will be dominated by the resonances of free fatty acids. Nevertheless, due to the high spectral range of approximately 200 ppm, the spectral resolution of carbon spectra is outstanding. The carbon resonances can be categorized in four groups, which are shown in **Table 6** [4]:

Resonance of nuclei in different CH groups			Resonance of nuclei adjacent to hydroxyl groups	Resonance of nuclei in lipids	Resonance of nuclei in carbonyl groups
$\delta \approx 25 - 60\,\text{ppm}$			$\delta \approx 60 - 100\,\text{ppm}$	$\delta \approx 20 - 50\,\text{ppm}$ and $\delta > 120\,\text{ppm}$	$\delta > 150\,\text{ppm}$
CH_3 groups	CH_2 groups	CH groups			
$\delta < 25\,\text{ppm}$	$\delta \approx 25 - 45\,\text{ppm}$	$\delta \approx 45 - 60\,\text{ppm}$			

Table 6. Chemical shifts of different ^{13}C moieties.

There are three techniques to increase the sensitivity of the ^{13}C nucleus. One is the application of cryogenic coils where the RF coil is actively cooled by coolant, for example, liquid nitrogen. This reduces the electrical resistance of the coil and increases the signal strength. Another way to increase sensitivity is the application of heteronuclear broadband decoupling. This method also simplifies the interpretation of the spectrum since the scalar coupling between ^{13}C and ^{1}H is lifted. Application of ^{13}C-labelled precursors does not only increase sensitivity. Furthermore, it enables the tracking of brain metabolites, such as glycogen and neurotransmitters [26].

Some examples of detectable metabolites and the chemical shifts of the single carbon atoms are listed in **Table 7** [4]. A very good example for the application of ^{13}C spectroscopy lies in the observation of glycogen regulation. This might have tremendous impact in the understanding

of pathologies such as diabetes mellitus. Tracking the metabolic pathways provides a unique information which can only be acquired with the use of ^{13}C spectroscopy.

Metabolite	Atom no.					
	1	2	3	4	5	6
γ-aminobutyric acid (GABA)	182.3	35.2	24.6	40.2	–	–
Glutamate	175.3	55.6	27.8	34.2	182.0	61.4
Glycogen	100.5	–	74.0	78.1	72.1	61.4
N-acetylaspartylglutamic acid (NAA)	179.7	54.0	40.3	179.7	174.3	22.8

Table 7. Chemical shifts (in ppm) of detectable carbon metabolites.

3.5. Functional phantoms and data interpretation

As shown in Section 3.1.4, the main advantage of MQ spectroscopy lies in its capability of recording signals from different coherences simultaneously. However, in order to connect the observed effect to a specific physiological response often remains difficult. In an *in vivo* experiment one has to face the fact that physiological parameters, such as the pH value, temperature, and ion concentrations are hardly, or even not at all accessible. What can be done is, of course, a set of experiments consisting of experiments under pathological conditions and experiments under standard conditions.

A solution to this problem may be found by conducting basic biological experiments, which are carried out on organotypic cell cultures. In contrast to *in vivo* experiments, organotypic cell cultures in microbioreactors provide a high degree of control over the experiment. Specific reactions can be initiated by adding drugs directly to the cell culture.

The principal approach of combining organotypic cell culture experiments in microbioreactors with MRI-detection techniques was impressively shown by Gottwald et al. [3]. In their study, Gottwald et al. used a MRI compatible bioreactor to perform contrast enhanced perfusion ^{1}H-MRI. The setup contained the MRI compatible reactor, which in turn contains a perfused three dimensional cell culture on a chip (3D-KITChip), an external perfusion system with medium supply, and a gas mixing station. It could be shown that the perfusion characteristics are nearly independent of the flow rates, and the system could be completely washed out from applied drugs or contrast agent. From this, it follows that every drug applied in the system will be washed out, allowing the cell culture to reach its initial state again. Basically, this system can serve as a *functional phantom* for the development and testing of new MR sequences, as well as for recording the specific response of cells to different drugs under various physiological conditions.

The bioreactor with a medium reservoir and a peristaltic pump is shown in **Figure 9a**. A cross section of the reactor with the flux of cell culture medium is depicted in **Figure 9b**. One can see that the medium enters the bioreactor housing from below the chip and is then pumped through the pores of the chip, and therefore through the tissue residing in the microcavities,

to the compartment above the tissue. The medium finally exits the bioreactor to the right side. By the use of this perfusion technique, the cells can be ideally supplied with medium and can be cultured organotypically for weeks. This setup can then be used to record MQ spectra from the cell culture. An example ^{23}Na-TQTPPI spectrum without cells, recorded with a custom built ^{23}Na surface coil at 9.4 T, is shown in **Figure 9c**. The SQ resonance is shown on the right side of the spectrum. It is not surprising that the SQ resonance is extremely large compared to the rest of the spectrum, since this resonance contains the complete amount of free ions. Higher frequencies are displayed from right to left. It should be noted that despite the DQ suppression, the DQ resonance was not suppressed completely. This is related to imperfection in the excitation pulses arising from the inhomogeneous pulse profile of the surface coil. A zoomed section (shown by the red box) of the spectrum is depicted in **Figure 9d**. As one can see, there is no TQ resonance at the expected frequency.
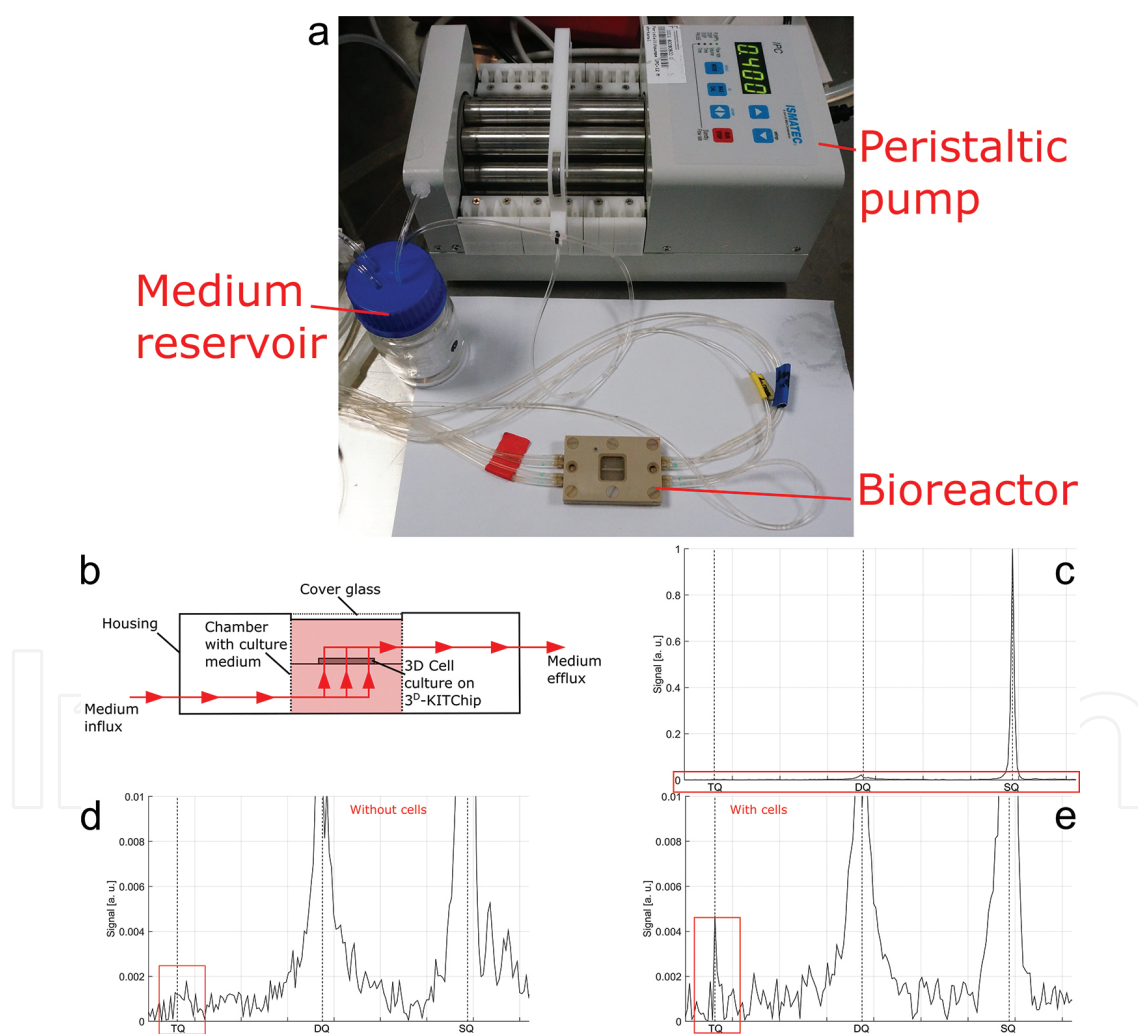

Figure 9. (a) Bioreactor with medium reservoir and peristaltic pump. (b) Cross section of the bioreactor with perfusion direction. (c) With custom built surface coil recorded complete ^{23}Na-TQTPPI spectrum of the bioreactor without cells at 9.4 T. (d) Zoomed section (red box in c) of the spectrum without cells. The spectrum shows no significant TQ contribution. (e) Zoomed section of a ^{23}Na-TQTPPI spectrum with cells. The TQ contribution is clearly present.

The situation changes critically when the experiment is repeated with an active cell culture. In **Figure 9d**, the zoomed section of a ^{23}Na-TQTPPI spectrum is shown from an experiment with a cell culture. One can clearly see the TQ resonance at the expected frequency. Compared to the other resonances, the TQ contribution is extremely small, but the quality of the gained information is revealed if one takes the dimensions of the experiment into account. In the very best case scenario, the entire fraction of the cell culture is approximately 1.2% of the complete volume under investigation. It is obvious that the TQ signal arises from this small fraction which proves that the TQTPPI spectroscopy is a very sensitive tool.

3.6. Conclusions

Based on their involvement in physiological processes such as energy metabolism, generation of action potentials and cell volume regulation, NMR experiments on X-nuclei can provide valuable physiological information.

On the one hand, there are nuclei with a nuclear spin equal to 1/2 which can be measured by means of pulse sequences known from ^{1}H-NMR. For instance, ^{31}P spectra can be generated by usage of simple single pulse sequences. Despite the relative low NMR sensitivity, the information obtained by the application of such simple sequences is always related to the biological background of the nucleus under investigation. On the other hand, for the exploitation of the full potential of spin 3/2 X-nuclei, their unique (quantum) physical properties must be utilised. Sequences capable to generate and record MQCs can be used to study changes in the motional freedom of the nuclei. In living systems, the motional freedom can be influenced by a change in ion binding or by morphological changes of the environment of the nucleus. Therefore, the analysis of MQCs in biological tissue can provide additional information about protein activity or changes in cell volume.

It is of high importance to link changes in the observed signal to the underlying physiological processes. The usage of functional phantoms is a very promising way to establish that link. Since the available magnetic field strength is continuously increasing, the relative low NMR sensitivity of these nuclei may no longer be a drawback in the future.

Author details

Eric Gottwald[1*], Andreas Neubauer[2] and Lothar R. Schad[2]

*Address all correspondence to: eric.gottwald@kit.edu

1 Institute for Biological Interfaces (IBG-5), Karlsruhe Institute of Technology, Karlsruhe, Germany

2 Computer Assisted Clinical Medicine, Medical Faculty Mannheim, Heidelberg University, Mannheim, Germany

References

[1] Konstandin S and Schad LR. 30 Years of Sodium/X-Nuclei Magnetic Resonance Imaging. Magn Reson Mater Phys. 2014;27:1–4.

[2] Konstandin S and Nagel AM. Measurement Techniques for Magnetic Resonance Imaging of Fast Relaxing Nuclei. Magn Reson Mater Phys. 2014;27:5–9.

[3] Gottwald E, Kleintschek T, Giselbrecht S, Truckenmüller R, Altmann B, Worgull M, Döpfert J, Schad LR and Heilmann M. Characterization of a Chip-Based Bioreactor for Three-Dimensional Cell Cultivation via Magnetic Resonance Imaging. Z Med Phys. 2013;23(2):102–110.

[4] de Graaf RA. In Vivo NMR Spectroscopy. 2nd ed. Chichester: John Wiley & Sons Ltd.; 2007. 570 p.

[5] Haacke EM, Brown RW, Thompson MR and Venkatesan R. Magnetic Resonance Imaging. Physical Principles and Sequence Design. John Wiley & Sons Ltd.; 1999. 914 p.

[6] Thulborn KR, Gindin TS, Davis D and Erb P. Comprehensive MR Imaging Protocol for Stroke Management: Tissue Sodium Concentration as a Measure of Tissue Viability in Nonhuman Primate Studies and in Clinical Studies. Radiology. 1999;213(1):156–166.

[7] Umathum R, Rösler MB and Nagel AM. In Vivo ^{39}K MR Imaging of Human Muscle and Brain. Radiology. 2013;269(2):569–576.

[8] Nagel AM, Lehmann-Horn F, Weber MA, Jurkat-Rott K, Wolf MB, Radbruch A, Umathum R and Semmler W. In Vivo ^{35}Cl MR Imaging in Humans: A Feasibility Study. Radiology. 2014;271(2):585–595.

[9] Fuller GF. Nuclear Spins and Moments. J Phys Chem Ref Data 1976;5(4):835–1092.

[10] Abragam A. Principles of Nuclear Magnetism. London: Oxford University Press; 1961. 599 p.

[11] van der Maarel JR. Thermal Relaxation and Coherence Dynamics of Spin 3/2 I. Static and Fluctuating Quadrupolar Interactions in the Multipole Basis. Concept Magn Reson A. 2003;19A(2):97–116.

[12] Dubbers D and Stöckmann H-J. Quantum Physics: The Bottom-Up Approach. From the Simple Two-Level System to Irreducible Representations. 1st ed. Heidelberg, Berlin: Springer-Verlag; 2013. 266 p. DOI: 10.1007/978-3-642-31060-7_1

[13] Rooney WD and Springer Jr CS. A Comprehensive Approach to the Analysis and Interpretations of Resonances of Spins 3/2 from Living Systems. NMR Biomed. 1991;4:209–226.

[14] Schepkin VD, Elumalai M, Kitchen JA, Qian C, Gor'kov PL and Brey WW. In Vivo Chlorine and Sodium MRI of Rat Brain at 21.1 T. Magn Reson Mater Phy. 2014;27(1): 63–70.

[15] Kirsch S, Augath M, Seiffge D, Schilling L and Schad LR. In Vivo Chlorine-35, Sodium-23 and Proton Magnetic Resonance Imaging of the Rat Brain. NMR Biomed. 2010;23:592–600.

[16] Ernst RR, Bodenhausen G and Wokaun A. Principles of Nuclear Magnetic Resonance in One and Two Dimensions. New York, NY: Oxford University Press Inc.; 2004. 610 p.

[17] van der Maarel JR. Relaxation of Spin Quantum Number S = 3/2 Under Multiple-Pulse Quadrupolar Echoes. J Chem Phys. 1991;94(7):4765–4775.

[18] Grant DM and Harris RK, editors. Encyclopedia of Nuclear Magnetic Resonance. 2nd ed. Chichester: John Wiley & Sons Inc.; 1996. 668 p.

[19] Schepkin VD, Odintsov BM, Litvak I, Gor'kov PL, Brey WW, Neubauer A and Budinger TF. Efficient Detection of Bound Potassium and Sodium Using TQTPPI Pulse Sequence. Proc Intl Soc Mag Reson Med. 2015;23:1930.

[20] Meyer RA, Kushmerick TR and Brown R. Application of ^{31}P-NMR Spectroscopy to the Study of Striated Muscle Metabolism. Am J Physiol Cell Ph. 1982;242(1):C1–C11.

[21] Kemp GJ, Meyerspeer M and Moser E. Absolute Quantification of Phosphorus Metabolite Concentration in Human Muscle in Vivo by ^{31}P MRS: A Quantitative Review. NMR Biomed. 2007;20:555–565.

[22] Ng TC, Evanochko WT, Hiramoto RN, Ghanta VK, Lilly MB, Lawson AJ, Corbett, TH, Durant JR and Glickson JD. [31]P Spectroscopy of In Vivo Tumors. J Magn Reson. 1982;49:271–286.

[23] Hoffmann SH, Begovatz P, Nagel AM, Umathum R, Schommer K, Bachert P and Bock M. A Measurement Setup for Direct 17O MRI at 7 T. Magn Reson Med. 2001;66:1109–1115.

[24] Zhu XH and Chen W. In Vivo Oxygen-17 NMR for Imaging Brain Oxygen Metabolism at High Field. Prog Nucl Mag Res Sp. 2011;59(4):319–335.

[25] Hopkins AL and Barr RG. Oxygen-17 Compounds as Potential NMR T2 Contrast Agents: Enrichment Effects of H217O on Protein Solutions and Living Systems. Magn Reson Med. 1987;4(4):399–403.

[26] Bachelard H. Landmarks in the Application of ^{13}C-Magnetic Resonance Spectroscopy to Studies of Neuronal/Glial Relationships. Dev Neurosci. 1998;20:277–288.